RSC Advances

PAPER

View Article Online
View Journal | View Issue

Cite this: *RSC Adv.*, 2020, **10**, 41272

A ZnO@ABS/TPU/$CaSiO_3$ 3D skeleton and its adsorption/photocatalysis properties for dye contaminant removal†

Mengli Zhang,[ab] Xinshu Xia,*[bc] Changlin Cao,[bc] Hun Xue,[bc] Yujin Yang,[bc] Wei Li,[bc] Qinghua Chen,[bd] Liren Xiao*[ab] and Qingrong Qian *[bc]

Received 1st August 2020
Accepted 23rd October 2020

DOI: 10.1039/d0ra06661c

rsc.li/rsc-advances

Both adsorption and photocatalysis are considered to be effective methods for removing organic contaminants from dye wastewater. In this study, the construction of 3D skeletons based on the nanoparticles ZnO and ABS/TPU/calcium silicate ($CaSiO_3$) (shortened as ATC) were fabricated *via* fused deposition molding (FDM) technology. Characterization by scanning electron microscopy (SEM), transmission electron microscope (TEM), X-ray diffraction (XRD), X-ray photoelectron spectroscopy (XPS) depicted that ZnO nanospheres had been successfully grown on the 3D skeleton surface with an enlarged specific surface area. As the results of the RhB adsorption and photocatalytic degradation experiments showed, the removal ratio of RhB onto the ZnO-ATC skeleton was as high as 97.94% and the synergistic effect of adsorption and photocatalysis greatly shortened the RhB degradation time under ultraviolet light irradiation. The nanocomposites synthesized in this study showed a significant removal ability for organic pollutants, and could effectively overcome the limitation of the secondary removal of photocatalysts.

1. Introduction

With the progress of technology, the associated environmental pollution has become a global problem affecting human life and health. In particular, the direct discharge of industrial, agricultural, and domestic water outlets into rivers is resulting in a decline in water quality. How to effectively remove the organic pollutants from wastewater has received much attention. Photocatalysis is an effective method for the treatment of organic pollutants. Compared with filtration or sedimentation, photocatalysis[1–3] directly decomposes pollutants into environmentally sound substances, which means it does not require complex post-treatment procedures, thus greatly reducing the operating cost in practical applications. Currently, semiconductor metal oxides are still the main photocatalysts in many processes, among which zinc oxide (ZnO, 3.37 eV)[4–6] has been widely used to degrade organic pollutants in wastewater due to its high photosensitivity, high stability, relatively low toxicity, and low synthesis temperature.[7,8] In addition, adjusting the precursor and reaction time is a simple way to control the structure size and morphology of ZnO, as is increasing the specific surface area and crystallinity, and synthesizing nanoparticles or a hierarchical assembly of nanoscale structures (the most effective form of metal oxides), which can provide a wide photo-response range because the electron–hole pairs improve the separation efficiency.[9]

However, nanosphere ZnO powder has the following problems, same as for most other photocatalysts: (i) a high recombination rate of photogenerated electron–hole pairs inhibits the photocatalytic efficiency,[10] (ii) a low concentration of organic dyes in wastewater will directly affect the contact with the photocatalysts,[11] (iii) powder agglomeration leads to an easy deactivation and difficulty in performing the separation and recovery, which limit its practical application.[12] To prepare a supported nano-ZnO photocatalyst for overcoming the above problems, a large specific surface area, strong adsorption performance, and improving the catalyst carrier function of the adsorbent can solve the problems related to the separation and recovery of the catalyst, and overcome the shortcomings of easy agglomeration along with the poor stability of the catalyst particles. It has been reported so far that ZnO loaded on various supports has certain adsorption effects, such as zeolite,[13] activated carbon,[14,15] clay,[16,17] and graphene.[18,19] Problems like (i) and (ii) above could be solved if the carrier could transfer photogenerated electrons and generate a substrate enrichment environment on the surface of the carrier-ZnO composite, which would improve the contact frequency of the target

[a]*College of Chemistry and Materials Science, Fujian Normal University, Fuzhou 350007, China. E-mail: xlr1966@fjnu.edu.cn*

[b]*Engineering Research Center of Polymer Green Recycling of Ministry of Education, Fujian Normal University, Fuzhou 350007, China. E-mail: qrqian@fjnu.edu.cn; xsxia@fjnu.edu.cn*

[c]*College of Environmental Science and Engineering, Fujian Normal University, Fuzhou 350007, China*

[d]*Fuqing Branch, Fujian Normal University, Fuzhou 350007, China*

† Electronic supplementary information (ESI) available. See DOI: 10.1039/d0ra06661c

pollutant with the ZnO. The removal efficiency of organic dyes, such as garnet green and Congo red, indeed has been proven, but most of the carriers are still powder, and problem (iii) above still exists for those cases. For problem (iii), Soomin Son *et al.*[20] grew ZnO on a polymer skeleton produced by 3D printing for the photocatalytic degradation of methylene blue dye for the secondary removal of nanoparticles. However, at present, there is few literature reports on simultaneously immobilized adsorbents and photocatalysts in 3D printing and the use of a 3D skeleton to achieve the synergistic effect of adsorption/photocatalysis to remove organic pollutants and solve problem (iii) above. Among these few reports, fused deposition molding (FDM),[21–23] as a 3D printing technology, has the advantages of low cost, automation, and customization, and gradually has become of interest in many interdisciplinary fields. In the past few years, the technology has been widely used in the preparation of catalytic, adsorbent, conductive, and other materials.[24–27] On the one hand, 3D printing technology can expand the coverage of the overall catalytic/adsorbing materials, and realize the macrostructure optimization and active component control of the material. On the other hand, it is beneficial to strengthening the mass transfer/heat transfer process in the adsorption and photocatalytic degradation reactions, and the operation is flexible and reliable, and so can meet the requirements for experimental research.

In this study, adsorbent–photocatalyst composites were prepared by 3D printing combined with a hydrothermal method. Due to the poor polarity of 3D skeleton materials and the lack of active sites for ZnO growth, the complex synthesis process has restricted its significant development and application. On this basis, we adopted a nano-ZnO catalyst for the construction of a $CaSiO_3$-assisted 3D printing skeleton by a hydrothermal method and used this to realize the synergistic removal of organic pollutants by photocatalysis and adsorption and eliminated the need for a secondary removal process of nanoparticles. The effects of the adsorbent type, ZnO loading, and surface groups on the adsorption and photocatalytic properties of the samples were studied, and the relationships between the structure and properties of the composites was analyzed.

2. Experimental section

2.1 Materials

Commercial ABS AG10AP was purchased from Taiwan Chemical Fiber Co. Ltd. TPU 5377A was obtained from Bayer of Germany. Microporous calcium silicate (CSH) with a size of 100 meshes was provided by Shanxi Yuzhu New Material Technology Co. Ltd. Zinc acetate dihydrate, citric acid monohydrate, and sodium hydroxide were provided by Sinopharm Chemical Reagent Co. Ltd (Shanghai, China). Rhodamine B (RhB) was obtained from Tianjin Fuchen Chemical Reagent Co. Ltd and was used without further purification.

2.2 Preparation of the ABS/TPU/$CaSiO_3$ 3D skeleton

The ABS and TPU pellets were dried at 80 °C for 12 h, and the CSH was dried at 100 °C for 12 h. The dried ABS, TPU, and CSH with mass ratios of 8 : 2 : 0 and 8 : 2 : 3 were mixed uniformly. Then, the mixtures were melt-extruded and granulated on a co-directional parallel twin screw extruder (MEDI-22/40, Guangzhou Putong Experimental Analysis Instrument Co., Ltd., China). The speed of the main screw was 190 rpm, and the temperatures of the various sections were set as 100 °C, 120 °C, 145 °C, 165 °C, 175 °C, 185 °C, 175 °C, 170 °C, 160 °C, and 140 °C, respectively. The obtained master batch was extruded into a filament with a diameter of 1.75 ± 0.5 mm on a desktop-grade filament extruder (C type, Shenzhen Misida Technology Co., Ltd., China). The extrusion temperatures were 175 °C and 185 °C, and the screw speed was 15 rpm. The ABS/TPU or ABS/TPU/$CaSiO_3$ filaments were obtained.

The model of the skeleton was designed using a 3D CAD program. Cura software was used to slice and set the various parameters. Then, the designed skeleton was fabricated on an FDM printer (M2030, Shenzhen Soongon Technology Co., Ltd., China) using the ABS/TPU or ABS/TPU/$CaSiO_3$ filaments as a raw material. The nozzle temperature was 200 °C, and the platform temperature was 80 °C. The printing speed was 80 mm s^{-1} with a layer thickness of 0.4 mm, 100% in-fill, and nozzle diameter of 0.40 mm. The obtained skeletons were denoted as AT and ATC.

2.3 Synthesis of ZnO nanosphere on the 3D skeleton surface

The ZnO@3D skeleton was synthesized by a hydrothermal method. First, 1.2 g citric acid monohydrate and 1.0 g zinc acetate dihydrate were dissolved in 60 mL deionized water and 20 mL 1 mol L^{-1} NaOH aqueous solution was slowly added under vigorous stirring to obtain a mixed suspension. The 3D skeleton was immersed into the solution for 60 min and then the mixture was placed in a 100 mL reactor. The reactor was put in an electric thermostatic blast drying oven (DHG-9070A, Shanghai Zhongyou Instrument Equipment Co., Ltd., China) and the hydrothermal reaction proceeded at 120 °C for 24 h. Finally, the obtained sample was washed by absolute ethanol and deionized water three times, respectively. The final samples were denoted as ZnO-AT and ZnO-ATC.

2.4 Characterization

The morphologies of the prepared samples were analyzed on a JSM-7500F scanning electron microscopy system (SEMJEOL, Japan) at an accelerating voltage of 5 kV and a Tecnai G2 F30 field emission transmission electron microscopy system (USA FEI) at an accelerating voltage of 300 kV. X-ray diffraction (Bruker D8 Phaser $\lambda = 0.179$ nm, Cu Kα radiation) was used to analyze the phase and crystallinity of the samples. XPS spectra were recorded using a ESCALAB Xi+ spectrometer employing a monochromated Al Kα X-ray source as described previously. The specific surface area of the skeleton was calculated by the Brunauer–Emmet–Teller (BET) method, while the Barrett–Joyner–Halen (BJH) method was applied to determine the pore size distribution based on the nitrogen adsorption–desorption isotherm at 77 K obtained on a Bayer BELSORP mini II.

2.5 Adsorption experiment

In batch parallel experiments, about 1.0 g of the samples were weighed and added to 50 mL, 50 mg L^{-1} RhB solution in Erlenmeyer flasks. The flasks were sealed and rotated at a speed of 250 rpm at the temperature of 25 °C in a thermostatic oscillator (HNY-200B, Tianjin Onuo Instrument Co., Ltd.). The residual RhB concentration in the solution at various adsorption times was measured based on the wavelength of 554 nm on an UV-vis spectrophotometer. All the experiments were carried out more than three times. The effects of the adsorbent and adsorption time on the removal rate and adsorption capacity were studied. The removal efficiency and adsorption amount were calculated using eqn (1) and (2), respectively:

$$R_e = \frac{C_0 - C_e}{C_0} \quad (1)$$

$$q = \frac{(C_0 - C_e)V}{M} \quad (2)$$

where R_e is the removal efficiency, q (mg g^{-1}) is the adsorption amount, C_0 (mg g^{-1}) is the initial concentration of RhB, C_e (mg g^{-1}) is the concentration of RhB solution at the completion of adsorption, V is the volume of the solution, and M is the weight of the sample.

2.6 Photocatalytic degradation experiment

The RhB photocatalytic degradation experiment was conducted in a 250 mL tubular quartz microreactor device. The reactor was surrounded by four 4 W UV lamps (4 W, 365 nm, Royal Philips Electronics of the Netherlands) used in tandem. The distance between the lamp tube and the reactor was about 3 cm, and the reaction temperature was controlled between 25 °C and 30 °C by air cooling.[28] Under UV irradiation, 1.0 g of the sample was added to 50 mL of RhB solution with an initial concentration of 50 mg L^{-1} for the photocatalytic degradation experiments. The RhB concentration was measured by a UV-vis spectrophotometer at the maximum absorption wavelength of 554 nm, and the degradation efficiency was calculated according to eqn (1). The effects of different initial dye concentrations and photocatalytic times on the degradation efficiency were investigated.

3. Results and discussion

3.1 Morphology studies

Fig. 1 displays the SEM surface morphologies of the 3D-printed skeleton and ZnO-3D-printed skeleton. Fig. 1b and d show that ATC skeleton and ZnO-ATC skeleton after the hydrothermal reaction. It was obvious that the surface of ZnO-ATC was uniformly coated with a layer of nanosphere crystals. By contrast, the AT skeleton without $CaSiO_3$ showed no significant change in the SEM images after the hydrothermal reaction, as shown in Fig. 1a and c. Thus, the $CaSiO_3$ played an important role in the growth of the ZnO on the skeleton surface.

As shown in the inset images of Fig. 1d, the ZnO had a flower-like morphology and its size was about 700 nm, which is consistent with the TEM result in Fig. 2a. Fig. 2b presents the HRTEM image of a single particle, in which obvious lattice fringes are visible with a spacing about 0.28 nm, corresponding to the (100) crystal face of ZnO. The elemental mapping (Fig. 2c–e) showed the existence of three elements, namely Zn, O, and Ca, while the uniform distribution of Ca elements indicated that Ca was doped in the ZnO lattice. These suggest that the formation of ZnO nanospheres on the ATC skeleton surface

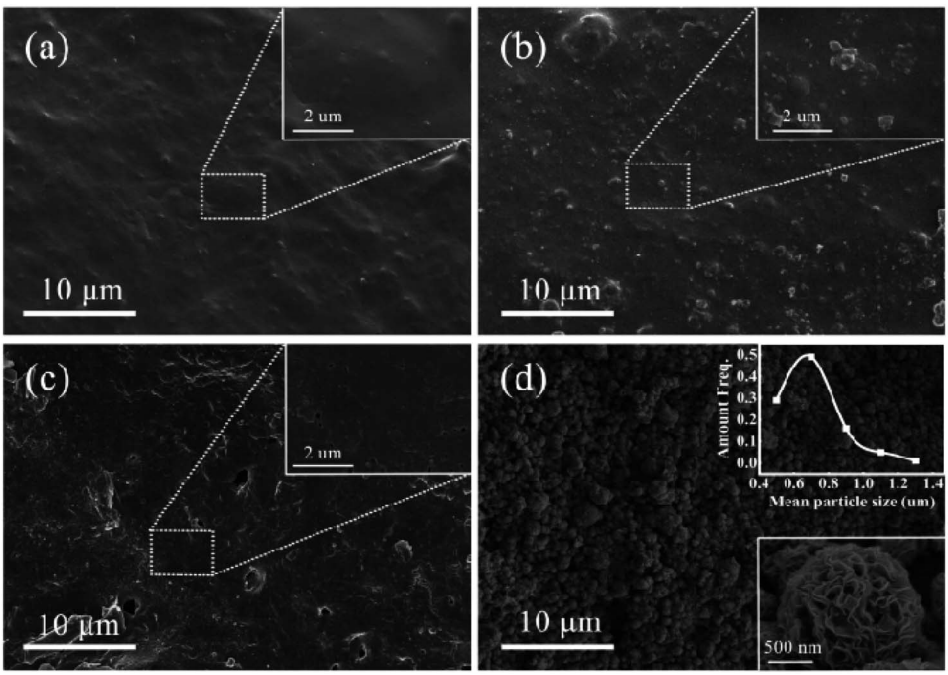

Fig. 1 SEM surface images of (a) AT, (b) ATC, (c) ZnO-AT, (d) ZnO-ATC.

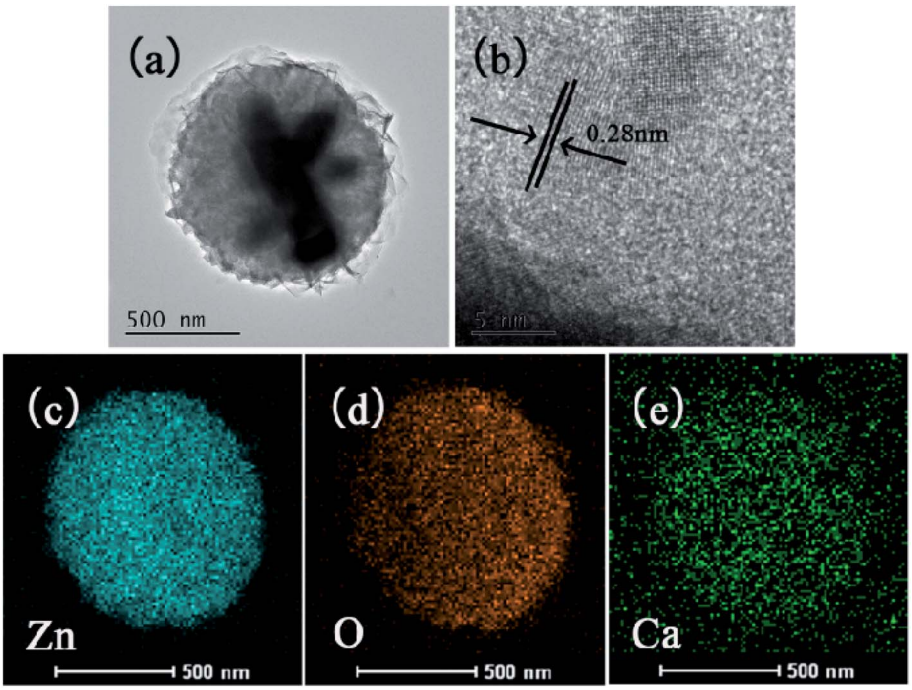

Fig. 2 TEM (a) and HRTEM (b) images of ZnO on the surface of ATC samples, and the corresponding elemental mapping results for Zn (c), O (d), Ca (e).

resulted from the large specific surface area of CSH and the large number of active sites on the 3D skeleton.[29,30] The presence of CSH enhanced the hydrophilicity of the skeleton surface and provided favorable conditions for the growth of ZnO on the skeleton surface.

3.2 XRD analysis

The phase and crystallinity of the synthetic composite samples could be found from the X-ray diffraction patterns. As shown in Fig. 3a, the wide diffraction peak at $2\theta = 23.70^\circ$ indicated the amorphous nature of ATC. The characteristic peak of AT before and after the hydrothermal reaction was almost the same, which indicated the unsuccessful growth of ZnO on the surface. According to the standardized PDF 00-029-0331 and JCPDS-36-1451, ATC corresponding to the (110) crystal plane at $2\theta = 29.2^\circ$ was the typical XRD diffraction peak of $CaSiO_3$.[31] The diffraction peaks of ZnO-ATC at $2\theta = 31.69^\circ$, 34.54°, 36.21°, 47.57°, 56.74° 62.95°, 66.43°, 67.88°, and 69.14° were consistent with the (1 0 0), (0 0 2), (1 0 1), (1 0 2), (1 1 0), (1 0 3), (2 0 0), (1 1 2), (2 0 1), and (2 0 2) orientation planes respectively,[17,32,33] suggesting that the crystal loaded on the skeleton surface was ZnO with a wurtzite structure. In addition, in the inset graph of Fig. 3a, the peak shift from $2\theta = 34.54^\circ$ to lower degrees was because of the ion size of Zn^{2+} (1.37 Å) and Ca^{2+} (1.97 Å). Also, it indicated that after the hydrothermal reaction, a small amount of Ca^{2+} was doped in the ZnO lattice due to the gradual dissolution process of Ca^{2+}.[34] The crystal morphology of ZnO clearly changed with the increased concentration of Ca^{2+} (Fig. S1†), which was beneficial to the formation of small nanospheres of ZnO with a grain size on the 3D skeleton surface.

3.3 XPS analysis

To further prove the composition of the nanocomposite, we performed X-ray electron spectroscopy (XPS) on the ATC and ZnO samples, and the results are shown in Fig. 3b–d. Fig. 4b shows the C spectra of the ATC and ZnO-ATC samples. There were two binding energies of C in ATC at 284.6 and 286 eV, which represented the hybrid orbitals of C–C and C–H from ABS and C–N from TPU in the skeleton. The evident emerging peak at 289.2 eV in the ZnO-ATC samples could be attributed to the formation of C=O bonds caused by the interaction between ZnO and the skeleton. Additionally, the broadened binding energy domain of each peak implied that multiple functional groups existed in ZnO-ATC, such as C–O, C=C, and C–O–C, which also indicated a strong interaction between the ZnO and the skeleton formed in the hydrothermal process.

Fig. 3c shows the O 1s spectrum of the ATC sample. The peak positions at 530.6, 531.9, and 533.4 eV were, respectively, attributed to Ca–O, O–Si, and O–C. Compared with ATC, the shift peak position of O element in the ZnO-ATC sample corresponded to the oxygen element in the surface lattice, while the oxygen element adsorbed on the surface was at 529.4 and 531.2 eV, respectively. Fig. 3d presents the Zn spectra of the ZnO-ATC samples. The two peaks at 1021.1 and 1044.2 eV belong to Zn $2p_{3/2}$ and Zn $2p_{1/2}$, respectively, which were almost consistent with the binding energy of pure ZnO. These results indicated that ZnO on the surface of ZnO-ATC had an excellent binding ability with the skeleton.

3.4 BET analysis

Fig. 4 shows the adsorption–desorption curves and pore-size distributions of the samples. In Fig. 4 and Table 1, the AT

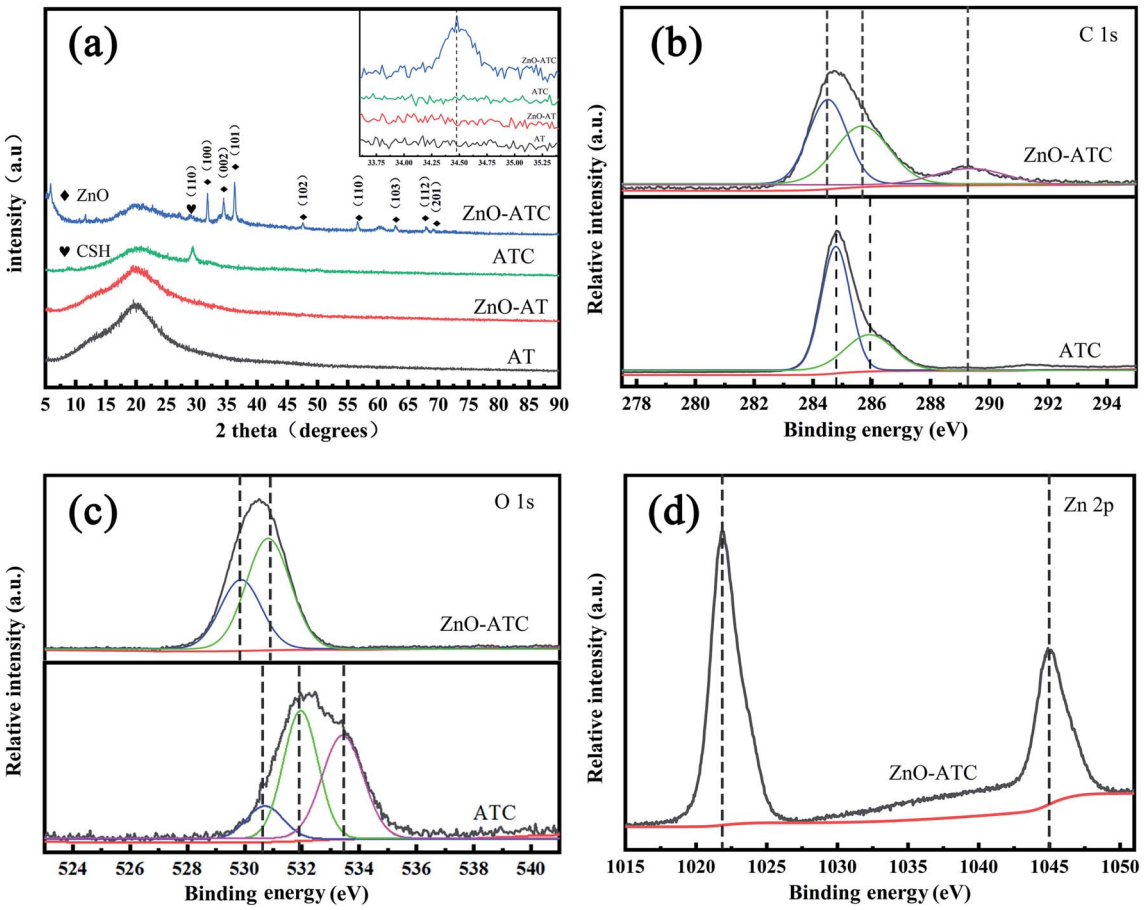

Fig. 3 (a)XRD peaks of the AT, ZnO-AT, ATC, and ZnO-ATC, XPS spectra of the ATC and ZnO-ATC, (b), (c), and (d) high-resolution spectra at C 1s, O 1s, and Zn 2p state energies, respectively.

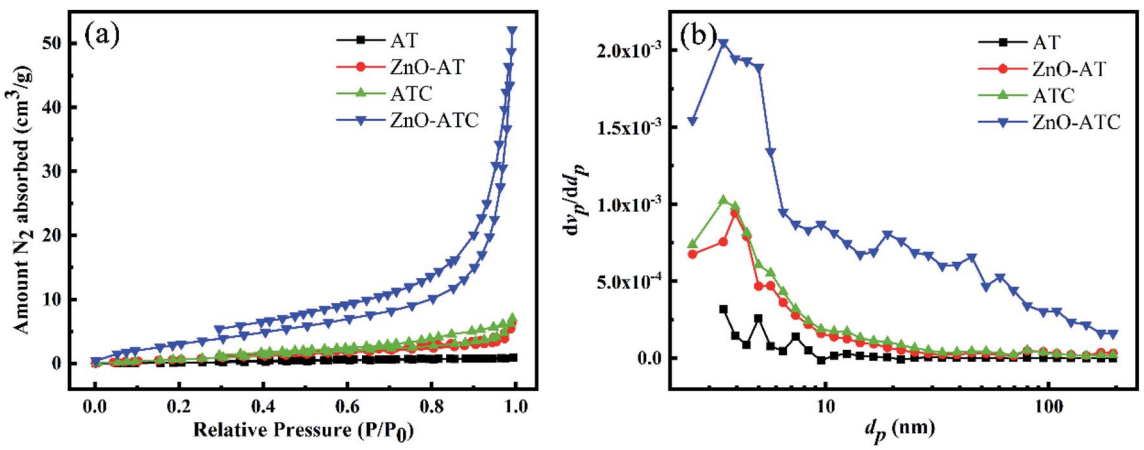

Fig. 4 (a) N_2 adsorption–desorption isotherms and (b) pore size distribution curves of AT, ZnO-AT, ATC and ZnO-ATC.

skeleton showed almost no pores and a low adsorption capability. ATC gave higher values in terms of the pore volume and specific surface area than AT because of the introduction of CSH in the 3D AT skeleton. Meanwhile, ZnO-ATC possessed the highest specific surface area, due to the presence of ZnO nanospheres affording a large number of adsorption sites. The

Table 1 Textural and structural properties of the samples

Sample	AT	ZnO-AT	ATC	ZnO-ATC
S_{BET} (m^2 g^{-1})	1.194	4.267	5.161	14.270
Total pore volume (cm^3 g^{-1})	0.001	0.010	0.010	0.077
Mean pore diameter (nm)	4.641	9.096	8.035	21.694

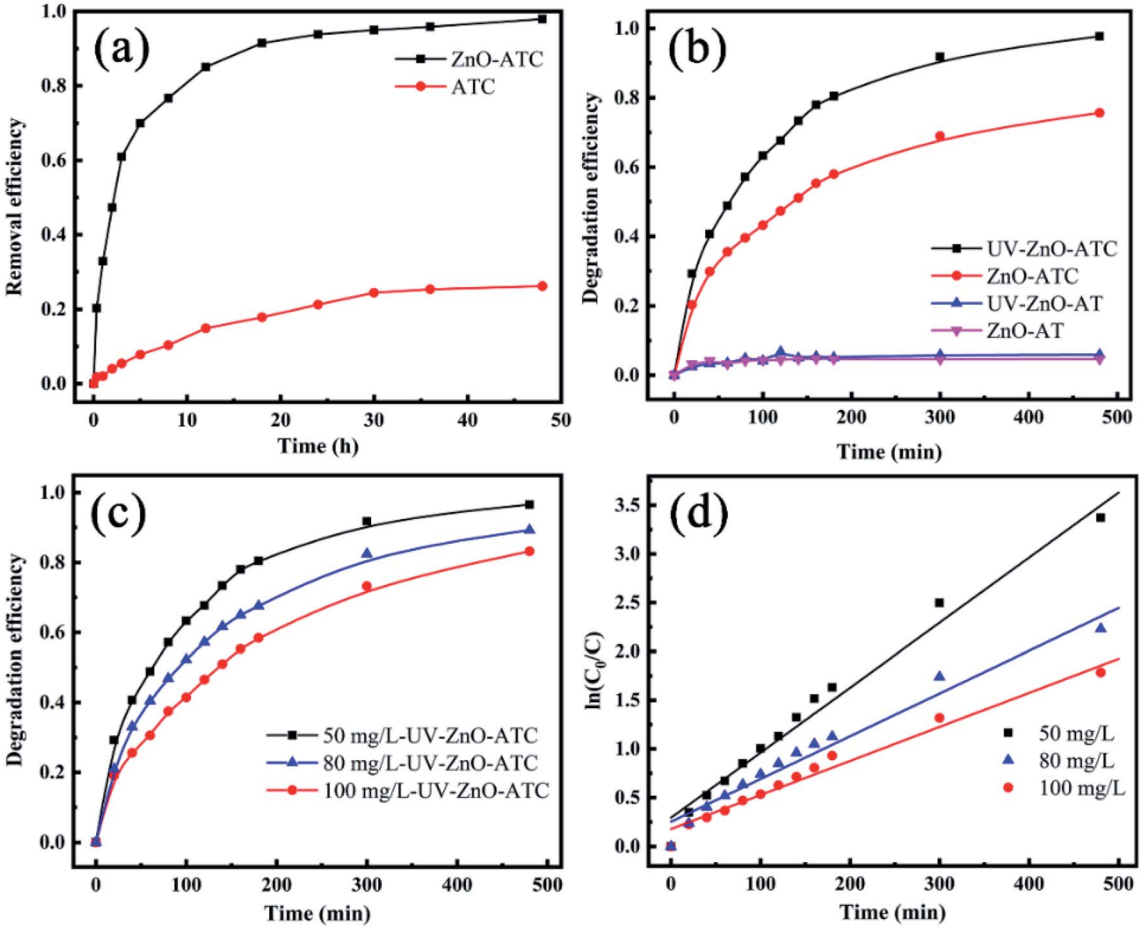

Fig. 5 (a) Removal efficiency curves of RhB onto AT and ATC (adsorbent concentration was 50 mg L^{-1} and temperature was 25 °C). (b) Degradation efficiency as a function of reaction time, under different materials for the 3D-skeleton for Rhodamine B (initial dye concentration = 50 mg L^{-1}). (c) Degradation kinetics and (d) pseudo-first-order rate constants of time under different initial dye concentrations.

N_2 isotherm of ZnO-ATC could be classified as a type II adsorption isotherm. It had only one inflection point in the initial stage, and the subsequent curve was concave, indicating that the adsorbent was a typical mesoporous material. The pore-size distribution of ZnO-ATC revealed that the pore sizes were in the range of 3–10 nm.

3.5 Adsorption

The RhB removal efficiency of the ATC and ZnO-ATC skeletons is given in Fig. 5a. It was clear that the RhB adsorption efficiency increased rapidly with the adsorption time and reached equilibrium at 24 h. The RhB adsorption efficiencies of ZnO-ATC and ATC at adsorption equilibrium were 97.94% and 26.22%, respectively. Therefore, the introduction of ZnO obviously increased the RhB adsorption capability of the 3D skeleton due to the improved specific surface area, pore volume, and adsorption affinity.

The adsorption includes the processes of membrane diffusion, diffusion of the adsorbate inside the particle, and the adsorption reaction. The slowest of the three steps determines the overall adsorption rate. Compared with the pseudo first order kinetics, the adsorption of ZnO-ATC and ATC adsorbents onto RhB showed higher fitting coefficients. It can be concluded that chemical adsorption was the determining process, which was caused by valence exchange and electron transfer between the adsorbate and adsorbent.[35,36] By further fitting the intra-particle diffusion model, it was found that ATC's adsorption of RhB took place in two steps. The first part was external surface adsorption, because of the high initial RhB concentration and large number of active adsorption sites. In the second part, until the equilibrium stage, the decreased adsorption rate determined the slow adsorption process and the intraparticle diffusion was further slowed down because of the decreased residual RhB concentration in the solution[37] (Fig. S2†).

3.6 Photodegradation

As shown in Fig. 5b, the degradation efficiency of RhB, composed of the photocatalytic degradation efficiency and absorption removal efficiency, gave different performances under the different 3D skeletons. In Fig. 5a, the ZnO-AT skeleton showed a low RhB degradation rate due to the absence of ZnO on its surface. The weak polarity and the absence of active sites caused a low loading amount of ZnO on the surface of the skeleton, resulting in its poor ability in adsorption and

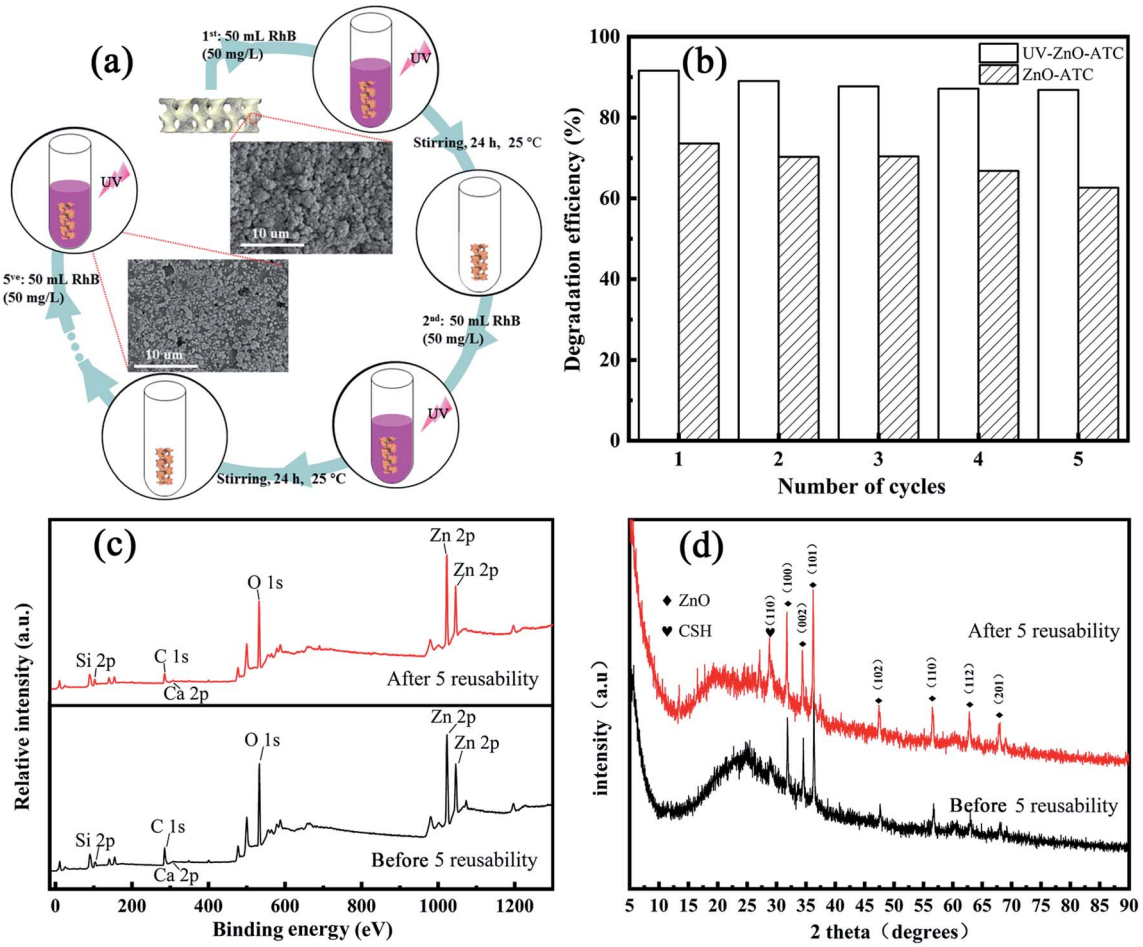

Fig. 6 (a) Schematic diagram of the 3D skeleton recycling. (b) Degradation efficiency after the reuse cycles. (c and d) XPS and XRD spectra from before and after 5 reusability cycles.

photodegradation of the dye. Compared with the condition of adopting UV irradiation for 8 h, the RhB removal efficiency of ZnO-ATC skeletons increased from 75.78% to 97.80%. Moreover, the equilibrium time shortened from 48 h to 8 h, indicating a synergistic effect occurred between the adsorption and photocatalytic degradation. The skeleton adsorption did not make the RhB enrichment environment closer to the skeleton, but rather it facilitated the ZnO on the skeleton surface to fully come into contact with the RhB dye molecules to promote the photocatalytic degradation process. In addition, due to the photocatalysis of ZnO, the dye concentration on the surface of the adsorbent decreased. Through the analysis of the adsorption process, it could be found that with the changing concentration on the surface of the adsorbent, the adsorption process will be prolonged to promote the adsorption process.

The degradation mechanism of RhB on the surface of ZnO-ATC skeleton was also studied and the results are given in Fig. 6. The pseudo-first-order model equation is as follows:

$$\ln\left(\frac{C_0}{C}\right) = kt \quad (3)$$

where, C_0 and C, respectively, represent the initial and post-reaction concentration of RhB dye, and k is the rate constant, expressing the degradation efficiency. The k values of ZnO-ATC were 0.00668, 0.00439, and 0.0035 at the RhB initial concentrations of 50, 80, and 100 mg L^{-1} (Fig. 5c), respectively. The degradation rate was reduced with the increasing RhB concentration due to the lower ratio of ZnO/RhB. Moreover, the increased concentration of pollutants brought about some intermediates to be adsorbed on the surface of the semiconductors. The slow diffusion of intermediates on the surface of semiconductors may lead to the deactivation of the active sites on semiconductors, and eventually reduce the degradation rate. These results observed are consistent with those obtained by other research groups.[14,34,38,39]

3.7 Reusability experiments

The stability and reusability of ZnO-ATC nanocomposites for RhB removal were investigated and the results are shown in Fig. 6. The adsorption and photocatalytic experiments were performed for 300 min. The adsorbent was separated and rinsed in deionized water for 24 h with a stirring speed of 200 rpm, and then dried at 70 °C for the next adsorption run.

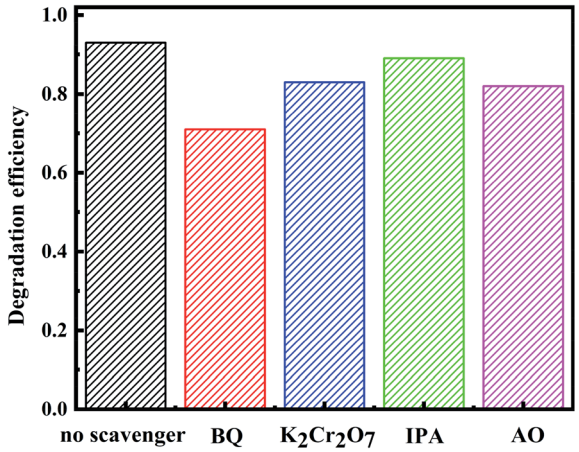

Fig. 7 Effects of different scavengers on the ZnO-ATC degradation efficiency.

The experiment was carried out for five runs. As shown in Fig. 6b, photocatalytic degradation efficiency showed a weak decrease, revealing the excellent stability, reusability, and recyclability of the ZnO-ATC 3D skeleton for RhB removal. The rate gradually decreased with the increasing runs was due to an incomplete desorption in the experimental process, destruction of the adsorption site, and partial detachment of ZnO on the surface of the skeleton. However, in general, the negligible decrease in the reusability property of the composites synthesized in this experiment was mainly due to the following two points. On the one hand, except for the inferior processability of the composite adsorbent, the improved adsorption performance of the skeleton resulted from the growth of ZnO, while the original performance could be maintained after desorption also mattered. On the other hand, it could be found for the adhesion of ZnO on the skeleton surface after five runs, as shown in Fig. 6a, that a layer of ZnO was still firmly adhered on the skeleton surface, which could meet the experimental requirements and so it displayed almost the same photocatalytic performance. Fig. 6b and d, respectively, present the XPS and XRD spectra before and after five runs, and the results clearly show that ZnO loaded on the 3D skeleton with a certain adsorption function could be detected and showed a strong combination and interaction.

3.8 Mechanism

The proposed mechanism is shown in Fig. 7, where the holes produced by electrons released from the valence band to the conduction band under UV radiation directly affect the photocatalytic activity of ZnO. The electrons in the conduction bands reduce oxygen molecules and release superoxide radicals, while the holes in the conduction bands react with hydroxyl ions to form hydroxyl radicals. These strong oxidant free radicals can convert organic dye molecules into CO_2 and H_2.[17] The role of ZnO in dye degradation can be expressed as per the following equations:[9,21,35]

$$ZnO + h\nu \rightarrow h^+(VB) + e^-(CB) \quad (4)$$

$$h^+(VB) + H_2O \rightarrow HO^\bullet + H^+ \quad (5)$$

$$h^+(VB) + OH^- \rightarrow HO^\bullet + H^+ \quad (6)$$

$$e^-(CB) + O_2 \rightarrow O_2^- \quad (7)$$

$$HO^\bullet/O_2^- + \text{organic pollutants} \rightarrow CO_2\uparrow + H_2O + \text{other degradation products} \quad (8)$$

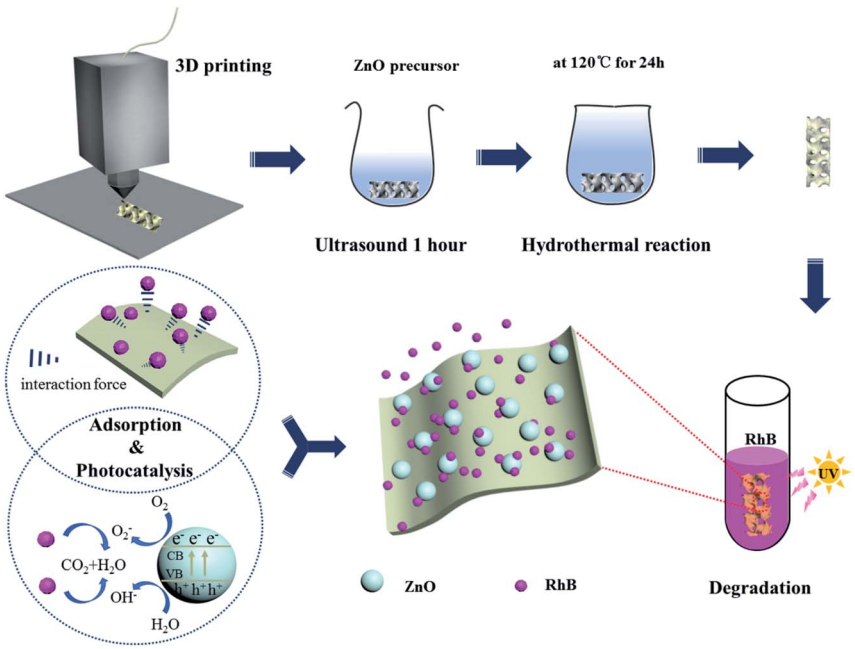

Fig. 8 Photocatalysis and adsorption mechanism of RhB on the surface of the 3D skeleton.

UV energy is higher than the band gap of ZnO and under the excitation of ultraviolet light, electrons are transferred from the valence band to the conduction band to form photoelectrons (e^-(CB)) and vacancies (h^+(VB)) in ZnO. The holes and electrons can react with H_2O, OH^-, and O_2 in the dye solution to form strong oxidizing $HO^\bullet$ and O_2^-, respectively. Reacting with organic dyes, raw water, carbon dioxide, and other degradation products are produced in different ways. The hydroxyl radical formed in ZnO degrades the organic dye RhB by strong oxidation. The main active radicals in the process of ZnO photocatalysis were investigated by free radical trapping experiments. As shown in Fig. 7, the degradation efficiency was inhibited by varying degrees to 70.8% (benzoquinone BQ), 81.4% (potassium dichromate $K_2Cr_2O_7$), 87.1% (ammonium oxalate IPA), and 79.6% (ammonium oxalate AO), respectively, which were lower than those without scavenger (93.2%) indicated that O_2^-, e^-, $HO^\bullet$ and h^+ played a role in the process of photocatalysis, the most obvious inhibitory effect of BQ indicates that the main free radical in the photocatalytic process was O_2^-.

Besides, the structure of the 3D printed skeleton was controllable, providing a relatively effective specific surface area and larger space. Therefore, the ZnO nanospheres could be loaded on the skeleton with a large specific surface area from the 3D printing contained CSH for the preferential adsorption and to form a RhB enrichment environment on the skeleton surface, which provided more opportunities for the diffusion of organic molecules and hydroxyl radicals and proton transfer. In the case of there being no skeleton, the RhB molecules collide with ZnO accidentally and remain in contact to carry out the photocatalytic reaction. If this requirement is not met, the dye molecules or intermediate products will return to the solution, and further reaction can only be carried out when they collide with ZnO again.[14] In this study, the adsorption effect of the skeleton combined with the photocatalytic activity of ZnO forms a synergistic effect, thus promoting the degradation of RhB (Fig. 8).

4. Conclusion

In this paper, an enhanced synergistic effect of photocatalytic and adsorption was realized through a system constructed of ZnO nanoparticle loaded onto a 3D skeleton. The system achieved the immobilization effect and promoted combination during the photocatalytic process. In contrast with the complex and harsh condition and atmosphere acquired, the facile reaction employing a hydrothermal technique eliminates the demanding requirement in the procedure for recycling and the 3D skeleton loaded with ZnO could be utilized repeatedly after a simple aftertreatment. Additionally, the diverse molecular design and structural control of the ZnO-ATC skeleton could enhance the application lifetime and its recycling life. Furthermore, a new strategy was proposed to make the adsorption and photocatalytic degradation work together and to realize the powder immobilization, which may pave the way for the design of new pollutant degradation materials and could be applied in the fields of wastewater treatment in large chemical equipment and plants.

Conflicts of interest

There are no conflicts to declare.

Acknowledgements

This work was financially supported by National Key Research and Development Program of China (2019YFC1904505) and National Natural Science Foundation of China (NSFC 21875037).

References

1 D. Ravelli, D. Dondi, M. Fagnoni and A. Albini, Photocatalysis. A multi-faceted concept for green chemistry, *Chem. Soc. Rev.*, 2009, **38**, 1999–2011.
2 S. Malato, P. Fernandez-Ibanez, M. I. Maldonado, J. Blanco and W. Gernjak, Decontamination and disinfection of water by solar photocatalysis: recent overview and trends, *Catal. Today*, 2009, **147**, 1–59.
3 D. F. Xu, B. Cheng, S. W. Cao and J. G. Yu, Enhanced photocatalytic activity and stability of Z-scheme Ag_2CrO_4-GO composite photocatalysts for organic pollutant degradation, *Appl. Catal., B*, 2015, **164**, 380–388.
4 A. Kolodziejczak-Radzimska and T. Jesionowski, Zinc Oxide-From Synthesis to Application: A Review, *Materials*, 2014, **7**, 2833–2881.
5 F. Lu, W. P. Cai and Y. G. Zhang, ZnO hierarchical micro/nanoarchitectures: solvothermal synthesis and structurally enhanced photocatalytic performance, *Adv. Funct. Mater.*, 2008, **18**, 1047–1056.
6 S. Marković, A. Stanković, J. Dostanić, L. Veselinović, L. Mančić, S. D. Škapin, G. Dražič, I. Janković-Častvan and D. Uskoković, Simultaneous enhancement of natural sunlight- and artificial UV-driven photocatalytic activity of a mechanically activated ZnO/SnO_2 composite, *RSC Adv.*, 2017, **7**, 42725–42737.
7 X. Q. Gu, C. Y. Li, S. Yuan, M. G. Ma, Y. H. Qiang and J. F. Zhu, ZnO based heterojunctions and their application in environmental photocatalysis, *Nanotechnology*, 2016, **27**, 402001.
8 S. M. Saleh, ZnO nanospheres based simple hydrothermal route for photocatalytic degradation of azo dye, *Spectrochim. Acta, Part A*, 2019, **211**, 141–147.
9 K. M. Lee, C. W. Lai, K. S. Ngai and J. C. Juan, Recent developments of zinc oxide based photocatalyst in water treatment technology: a review, *Water Res.*, 2016, **88**, 428–448.
10 C. Gomez-Solis, J. C. Ballesteros, L. M. Torres-Martinez, I. Juarez-Ramirez, L. A. D. Torres, M. E. Zarazua-Morin and S. W. Lee, Rapid synthesis of ZnO nano-corncobs from Nital solution and its application in the photodegradation of methyl orange, *J. Photochem. Photobiol., A*, 2015, **298**, 49–54.

11 R. Leary and A. Westwood, Carbonaceous nanomaterials for the enhancement of TiO_2 photocatalysis, *Carbon*, 2011, **49**, 741–772.
12 B. Wang, G. X. Zhang, X. Leng, Z. M. Sun and S. L. Zheng, Characterization and improved solar light activity of vanadium doped TiO_2/diatomite hybrid catalysts, *J. Hazard. Mater.*, 2015, **285**, 212–220.
13 A. Nezamzadeh-Ejhieh and S. Khorsandi, Photocatalytic degradation of 4-nitrophenol with ZnO supported nano-clinoptilolite zeolite, *J. Ind. Eng. Chem.*, 2014, **20**, 937–946.
14 P. Muthirulan, M. Meenakshisundararam and N. Kannan, Beneficial role of ZnO photocatalyst supported with porous activated carbon for the mineralization of alizarin cyanin green dye in aqueous solution, *J. Adv. Res.*, 2013, **4**, 479–484.
15 M. Ghaedi, A. Ansari, M. H. Habibi and A. R. Asghari, Removal of malachite green from aqueous solution by zinc oxide nanoparticle loaded on activated carbon: kinetics and isotherm study, *J. Ind. Eng. Chem.*, 2014, **20**, 17–28.
16 S. C. Motshekga, S. S. Ray, M. S. Onyango and M. N. B. Momba, Microwave-assisted synthesis, characterization and antibacterial activity of Ag/ZnO nanoparticles supported bentonite clay, *J. Hazard. Mater.*, 2013, **262**, 439–446.
17 H. B. Hadjltaief, S. Ben Ameur, P. Da Costa, M. Ben Zina and M. E. Galvez, Photocatalytic decolorization of cationic and anionic dyes over ZnO nanoparticle immobilized on natural Tunisian clay, *Appl. Clay Sci.*, 2018, **152**, 148–157.
18 T. G. Xu, L. W. Zhang, H. Y. Cheng and Y. F. Zhu, Significantly enhanced photocatalytic performance of ZnO via graphene hybridization and the mechanism study, *Appl. Catal., B*, 2011, **101**, 382–387.
19 B. J. Li and H. Q. Cao, ZnO@graphene composite with enhanced performance for the removal of dye from water, *J. Mater. Chem.*, 2011, **21**, 3346–3349.
20 S. Son, P. H. Jung, J. Park, D. Chae, D. Huh, M. Byun, S. Ju and H. Lee, Customizable 3D-printed architecture with ZnO-based hierarchical structures for enhanced photocatalytic performance, *Nanoscale*, 2018, **10**, 21696–21702.
21 G. H. Wu and S. H. Hsu, Review: Polymeric-Based 3D Printing for Tissue Engineering, *J. Med. Biol. Eng.*, 2015, **35**, 285–292.
22 S. C. Ligon, R. Liska, J. Stampfl, M. Gurr and R. Mulhaupt, Polymers for 3D Printing and Customized Additive Manufacturing, *Chem. Rev.*, 2017, **117**, 10212–10290.
23 K. S. Boparai, R. Singh and H. Singh, Development of rapid tooling using fused deposition modeling: a review, *Rapid Prototyp. J.*, 2016, **22**, 281–299.
24 X. T. Zhou and C. J. Liu, Three-dimensional Printing for Catalytic Applications: Current Status and Perspectives, *Adv. Funct. Mater.*, 2017, **27**, 1701134.
25 J. C. Ruiz-Morales, A. Tarancon, J. Canales-Vazquez, J. Mendez-Ramos, L. Hernandez-Afonso, P. Acosta-Mora, J. R. M. Rueda and R. Fernandez-Gonzalez, Three dimensional printing of components and functional devices for energy and environmental applications, *Energy Environ. Sci.*, 2017, **10**, 846–859.
26 M. Czolderova, M. Behul, J. Filip, P. Zajicek, R. Grabic, A. Vojs-Stanova, M. Gal, K. Kerekes, J. Hives, J. Ryba, M. Rybanska, P. Brandeburova and T. Mackul'ak, 3D printed polyvinyl alcohol ferrate(VI) capsules: effective means for the removal of pharmaceuticals and illicit drugs from wastewater, *Chem. Eng. J.*, 2018, **349**, 269–275.
27 S. Shi, Y. Chen, J. Jing and L. Yang, Preparation and 3D-printing of highly conductive polylactic acid/carbon nanotube nanocomposites via local enrichment strategy, *RSC Adv.*, 2019, **9**, 29980–29986.
28 H. Xue, Z. Li, L. Wu, Z. Ding, X. Wang and X. Fu, Nanocrystalline ternary wide band gap p-block metal semiconductor $Sr_2Sb_2O_7$: hydrothermal syntheses and photocatalytic benzene degradation, *J. Phys. Chem. C*, 2008, **112**, 5850–5855.
29 W. Guan, F. Y. Ji, Q. K. Chen, P. Yan and Q. Zhang, Preparation and phosphorus recovery performance of porous calcium-silicate-hydrate, *Ceram. Int.*, 2013, **39**, 1385–1391.
30 S. L. Ding, D. X. Fang, Z. S. Pang, B. Luo, L. Kuang, H. Wang, Q. Zhang, Q. S. Shen and F. Y. Ji, Immobilization of powdery calcium silicate hydrate via PVA covalent cross-linking process for phosphorus removal, *Sci. Total Environ.*, 2018, **645**, 937–945.
31 B. Lothenbach, D. Nied, E. L'Hopital, G. Achiedo and A. Dauzeres, Magnesium and calcium silicate hydrates, *Cem. Concr. Res.*, 2015, **77**, 60–68.
32 L. Xu, Y. L. Hu, C. Pelligra, C. H. Chen, L. Jin, H. Huang, S. Sithambaram, M. Aindow, R. Joesten and S. L. Suib, ZnO with Different Morphologies Synthesized by Solvothermal Methods for Enhanced Photocatalytic Activity, *Chem. Mater.*, 2009, **21**, 2875–2885.
33 M. Sharma, M. Joshi, S. Nigam, S. Shree, D. K. Avasthi, R. Adelung, S. K. Srivastava and Y. Kumar Mishra, ZnO tetrapods and activated carbon based hybrid composite: Adsorbents for enhanced decontamination of hexavalent chromium from aqueous solution, *Chem. Eng. J.*, 2019, **358**, 540–551.
34 B. Santoshkumar, S. Kalyanaraman, R. Vettumperumal, R. Thangavel, I. V. Kityk and S. Velumani, Structure-dependent anisotropy of the photoinduced optical nonlinearity in calcium doped ZnO nanorods grown by low cost hydrothermal method for photonic device applications, *J. Alloys Compd.*, 2016, **658**, 435–439.
35 C. Li, Y. He, L. Zhou, T. Xu, J. Hu, C. Peng and H. Liu, Fast adsorption of methylene blue, basic fuchsin, and malachite green by a novel sulfonic-grafted triptycene-based porous organic polymer, *RSC Adv.*, 2018, **8**, 41986–41993.
36 V. P. Jejurkar, G. Yashwantrao and S. Saha, Tröger's base functionalized recyclable porous covalent organic polymer (COP) for dye adsorption from water, *New J. Chem.*, 2020, **44**, 12331–12342.
37 C. Song, H. Li and Y. Yu, Homologous–heterogeneous structure control and intelligent adsorption effect of a polycationic gel for super-efficient purification of dyeing wastewater, *RSC Adv.*, 2019, **9**, 9421–9434.

38 H. Bel Hadjltaief, S. Ben Ameur, P. Da Costa, M. Ben Zina and M. Elena Galvez, Photocatalytic decolorization of cationic and anionic dyes over ZnO nanoparticle immobilized on natural Tunisian clay, *Appl. Clay Sci.*, 2018, **152**, 148–157.

39 A. Balcha, O. P. Yadav and T. Dey, Photocatalytic degradation of methylene blue dye by zinc oxide nanoparticles obtained from precipitation and sol-gel methods, *Environ. Sci. Pollut. Res.*, 2016, **23**, 25485–25493.

